On the 3D global dynamics of terrestrial bow-shock rippling in a quasi-perpendicular interaction with steady solar wind

Emanuele Cazzola, D. Fontaine, P. Savoini

HAL Id: hal-04167805
https://hal.sorbonne-universite.fr/hal-04167805

Submitted on 21 Jul 2023

On the 3D Global Dynamics of Terrestrial Bow-Shock Rippling in a Quasi-Perpendicular Interaction with Steady Solar Wind

E. Cazzola[1], D. Fontaine[1], and P. Savoini[1]

[1]Laboratoire de Physique des Plasmas (LPP), CNRS, Observatoire de Paris, Sorbonne Université, Université Paris-Saclay, École Polytechnique, Institut polytechnique de Paris, Palaiseau, 91120, France

Abstract

The phenomenon of bow-shock surface rippling has been studied throughout multidimensional simulations of ad hoc planar shock fronts. However, the investigation of global bow-shock behaviour with a 3D curved scenario has been poorly addressed thus far. In this work, we present an analysis of this scenario occurring during a low-β quasiperpendicular interaction with the interplanetary magnetic field by means of kinetic 3D computer simulations. The analysis was carried out with 3D hybrid simulations properly set to reproduce the interaction between solar wind and a realistic near-Earth environment. We have found that the ripples behave as IMF-perpendicular elongated structures extending along the bow-shock meridian plane and propagating parallel to the IMF orientation from the nose towards the flanks with a constant velocity (in the case studied here $\sim$ 8 times the upstream Alfvén speed). We have also confirmed that these ripples feature a broad range of wavelengths along the entire travel path, as locally observed with past simulations and observations (in this case $\geq$ 8 d_i). Moreover, from a kinetic analysis of the velocity distribution across the bow-shock nose, we have observed global signatures of the occurrence of shock-front reformation. We suggest that, among other kinetic mechanisms, shock-front reformation in the nose region can play an important role in the perturbation of the bow-shock surface, leading to the generation of modulations ultimately propagating along the bow-shock surface as MHD waves.

Keywords: 3D Bow-Shock Surface Rippling, Bow-Shock Shock-Front Reformation, 3D Global Bow-Shock Hybrid Simulation

1

1   Introduction

The terrestrial bow-shock constantly interacts with the solar wind at different conditions in terms of density, velocity and plasma β (i.e., ratio between thermal and magnetic energy), as well as with different intensities and directions of the interplanetary magnetic field (IMF). Particularly relevant is the interaction angle $\theta_{\mathbf{B}\hat{\mathbf{n}}}$ between the IMF and the local bow-shock normal direction: (i) when $0° < \theta_{\mathbf{B}\hat{\mathbf{n}}} < 45°$ the interaction belongs to the quasiparallel regime, (ii) when $45° < \theta_{\mathbf{B}\hat{\mathbf{n}}} < 90°$ to the quasiperpendicular regime. It has been discovered that, in the quasiperpendicular regime under supercritical conditions, shock surfaces show unstable behaviour leading to intense rippling of the shock surface. Shock surface rippling was also confirmed by recent observations in the terrestrial bow-shock with in situ satellites crossings (e.g., with the Magnetospheric Multiscale Mission (MMS) (Johlander et al., 2016; Madanian et al., 2021) and CLUSTER (Moullard et al., 2006; Lobzin et al., 2007)).

This phenomenon has long been studied with ad hoc multidimensional simulations of planar shock configurations, finding that the rippling manifests mainly for incoming solar wind Alfvénic Mach numbers and plasma β values beyond certain thresholds (Hellinger and Mangeney, 1997), and span a broad range of scales (Ofman and Gedalin, 2013): ions scale (~ 1 d_i (Lembege and Savoini, 1992)), intermediate-to-large scales ($\sim 6 - 8$ d_i (Winske and Quest, 1988; Lowe and Burgess, 2003; Burgess and Scholer, 2007) and ~ 20 d_i (Yuan et al., 2009)), or very large scales (> 100 d_i (Krauss-Varban et al., 2008)), d_i being the ion inertial length. Regarding the possible triggering mechanisms, Yang et al. (2012) suggested dividing those proposed to date in two main groups: (i) as caused by processes occurring along the shock surface, such as cross-field current instabilities (Lembege and Savoini, 1992), oblique whistler waves at the shock-front (Hellinger et al., 1996; Hellinger and Mangeney, 1997; Krasnoselskikh et al., 2002; Lembège et al., 2009), instabilities caused by downstream thermalisation processes, such as either Alfvénic Ion Cyclotron (AIC) or mirror instability (Tanaka et al., 1983; Winske and Quest, 1988) or the gyrating dynamics of reflected ions (Burgess and Scholer, 2007), or by free energy transfers at the shock front exciting MHD-like surface-wave modes, yet not excluding kinetic mechanisms as possible source (Lowe and Burgess, 2003), and (ii) as caused by normal-aligned phenomena, such as shock-front reformation (e.g., Lembege and Savoini (1992)).

All the aforementioned analyses mainly studied this phenomenon with ad hoc multidimensional simulations of a planar shock configuration with the incident velocity perfectly perpendicular to the shock front. Such a configuration well describes the situation when the interaction between solar wind and bow-shock is confined to a small region that can be considered almost planar. However, questions remain regarding how a realistic curved bow-shock may possibly behave

when subjected to a directional solar wind and to a magnetic configuration evolving from a planar to a significantly oblique interaction within the same connected global system. In fact, global 3D simulations of a quasiperpendicular interaction between the IMF and a realistic curved bow-shock are still poorly addressed in the literature. Recently, 3D global simulations of the entire geomagnetic environment have been performed in a more generic scenario to study the interplays between quasiparallel generated foreshock, magnetosheath turbulence and magnetic reconnection at the magnetopause (Karimabadi et al., 2014). Nevertheless, an analysis of the rippling process was not the aim of that work. More recently, Omidi et al. (2021) performed an analysis of the bow-shock rippling with 2.5D hybrid simulations in a curved configuration interacting with solar wind at a very high Mach number. Even though in these simulations the dynamics are still limited to a 2D global view, i.e., the effects of kinetic instabilities on the bow-shock dynamics at latitudes far from the magnetic equatorial plane cannot be inferred, it still confirms the presence of intense rippling on the bow-shock surface at more global scales, as well as that ripples can be detected even with relatively coarse resolution (their resolution was on the order of ion skin depth).

As such, in this work, we aim to provide more insights into the global quasiperpendicular rippling dynamics in a realistic three-dimensional curved bow-shock configuration under a relatively high Alfvénic Mach number scenario by means of 3D hybrid simulations. Particularly, we analyse the case of an IMF lying into the plane perpendicular to the Sun-Earth GSE X-coordinate. The analysis of more complicated configurations with the perpendicular interaction point located in other positions of the bow-shock surface will be left for future works. With the hybrid formalism, we are able to simulate a large portion of the bow-shock surface within a reasonable computational time by retaining the relevant kinetic information necessary to link the macroscopic scale with the kinetic scale. In particular, we want to investigate the global characteristics of the ripples, including their position, shape and propagation pattern, as well as the presence of kinetic mechanisms possibly contributing to their origins and compare such dynamics with those generated at a low Alfvénic Mach number.

The paper is structured as follows: Sections 2 and 3 introduce the setup and the methodology used to present the results in Section 4, while discussion of these results and conclusions are given in Section 5.

2   Simulation Setup

2.1   Numerical Setup

For the simulations shown here, we have adapted the 3D multispecies MPI-parallelized hybrid code LatHyS described in Modolo et al. (2005), which was already successfully used to study the interaction of magnetic clouds with the terrestrial bowshock (Turc et al., 2015), as well as the interaction of solar wind with the environments of Mars (Modolo et al., 2016; Romanelli et al., 2018), Mercury (Richer et al., 2012) and Venus (Aizawa et al., 2022). The code is based on the widely used hybrid CAM-CL scheme proposed in Matthews (1994). The ions are treated kinetically, whereas the electrons are treated as a fluid with an adiabatic description.

The simulation box is based on a 3D Cartesian grid with open boundary conditions on the left and right boundaries and periodic boundary conditions on the other edges. The solar wind enters the system homogeneously from the left boundary and uniformly flows towards the right boundary along the X-axis. All the outputs will be shown in GSE coordinates, unless clearly specified. Geomagnetic inclination of the terrestrial magnetic field is neglected, so that the GSE coordinates actually coincide with the GSM coordinates.

All the simulations feature a box size of $(150 \times 320 \times 400)$ d_i with a space resolution of $\Delta x = \Delta y = \Delta z = 1$ d_i, where d_i is the ion skin depth of the pristine solar wind. The time step adopted is $\Delta t = 0.005$ $\omega_{ci}^{-1} \sim 8.4 \cdot 10^{-3}$ s, ω_{ci} being the ion cyclotron frequency, while the magnetic field is advanced with a substepped time resolution of $\frac{\Delta t}{4}$. Only protons were considered in this analysis. The simulations for the parametric study feature 20 particles per cell, whereas the simulations selected for the ripples dynamics analysis feature 60 particles per cell. All the values are normalised to the pristine solar wind conditions. As a reference, in the cases studied in this work with an Alfvénic Mach number varying from $M_A = 3.87$ to $M_A = 9.50$, the ion skin depth varies from $d_i = 133.9$ km to $d_i = 123.6$ km, respectively. The scenario with $M_A = 9.50$ has also been simulated with a much higher space and time resolution in the magnetic equatorial plane to study local-scale kinetic effects (see Section 4.3), namely with a space resolution of $\Delta x = \Delta y = 0.2$ d_i and $\Delta z = 4$ d_i (the box size has been kept fixed to $150 \times 320 \times 400$ d_i, i.e., the number of cells is now $750 \times 1600 \times 100$) and a time resolution of $\Delta t = 5 \cdot 10^{-4}$ $\omega_{ci}^{-1} \sim 8.4 \cdot 10^{-4}$ s.

The near-Earth environment, i.e., the bow-shock and magnetopause boundaries, is self-consistently generated by setting up a magnetised dipole-like object within the simulation box with the dipolar magnetic moment oriented along $-Z$ to represent the terrestrial dipole orientation. The dipolar magnetic field progressively grows in intensity over the first cycles to smoothly achieve its steady-state

4

conditions. This object represents an inner boundary containing the Earth and is set to conveniently simulate a curved near-Earth environment. The object was scaled to a radius of 10 d_i, with a dipolar magnetic moment of 10^{-6} Tm^3. This approach allows us to correctly represent the terrestrial geomagnetic environment by reducing the overall computational costs compared to a full-scale simulation. The validity of this approach is supported by the conclusions drawn in Omidi et al. (2004), which showed that a realistic terrestrial environment is correctly simulated provided the magnetopause stand-off distance is greater than 20 d_i. Moreover, the resulting bow-shock shape has been successfully validated with predictive empirical models, such as that proposed in Jeřáb et al. (2005), Wang et al. (2015, 2020) and Kotova et al. (2021).

The interplanetary magnetic field (IMF) direction is fixed to generate a pure quasiperpendicular interaction with the bow-shock (BS) nose along the Y-axis, with the angle between the IMF and the bow-shock normal at the nose being $\theta_{\mathbf{B}\hat{\mathbf{n}}} = 90°$, i.e., $\mathbf{B} = B_y \hat{\mathbf{e}}_y$ and $B_x = B_z = 0$.

2.2 Data Input for the Alfvén Mach number Parametric Study

We first conducted a parametric study to identify the best scenarios to study the ripple dynamics. We selected a number of solar wind conditions with an increasing Alfvénic Mach number based on the values from the NASA OMNI website [1], summarised in Table 1. Notice that the case 4 with $M_A = 6.56$ represents the solar wind conditions studied in Johlander et al. (2016). All the simulations have been performed by fixing $\beta = 0.4$ and a quasiperpendicular shock configuration with the IMF perpendicular to the normal direction at the nose (along Y_{GSE}). The results are plotted in Figure 1.

2.3 Data Input for the Ripple Dynamics Analysis

From the outputs shown in Figure 1, we observe that rippling appears at approximately $M_A \geq 5$, with the strongest signature being in the case with $M_A = 9.50$. As such, this latter case has been considered for ripple dynamics analysis. This outcome has also been compared with a scenario with no ripples, such as that with $M_A = 3.87$.

3 Rippling Diagnostic Technique

To gain insights into ripple dynamics, we have performed an analysis similar to that done in Burgess and Scholer (2007). However, unlike the case studied in their

---

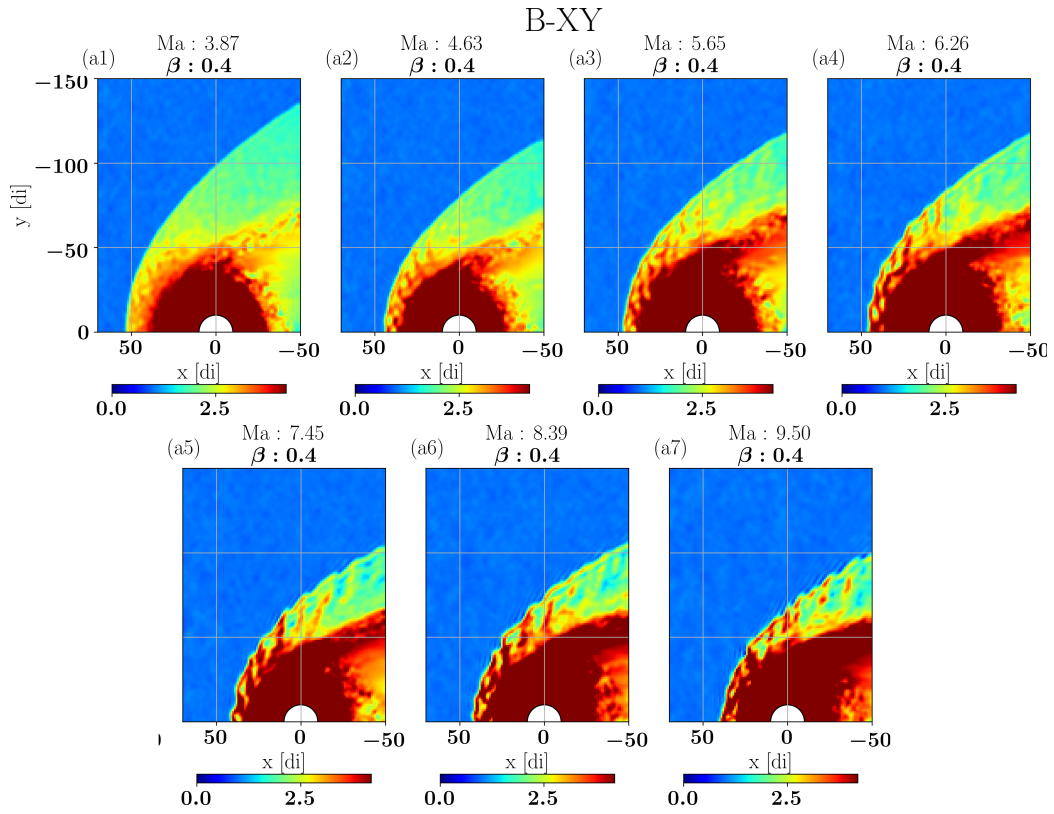[1]https://omniweb.gsfc.nasa.gov/form/dx1.html

Figure 1: Magnetic field intensity maps on half of the magnetic equatorial plane (as 3D data output cross-sections) for the parametric study cases in Table 1. The white disk represents the inner boundary of the domain (see explanation in the setup section). Values normalised to the solar wind upstream conditions.

Case	Year-DOY	Ma	B [nT]	N [cm^{-3}]	V [km s^{-1}]
1	2019-132	3.87	6.9	2.9	342
2	2019-131	4.63	9.7	7.7	353
3	2019-70	5.65	5.6	4.1	341
4	Johlander et al. (2016)	6.56	16.0	29.0	425
5	2019-5	7.45	6.7	5.0	487
6	2019-11	8.39	5.1	4.3	450
7	2019-244	9.50	6.2	3.4	697

Table 1: Summary of the Solar Wind conditions simulated in this work. The second column is the Day-of-Year DOY on which the Solar Wind data have been observed, the third column is the Alfvénic Mach number, the other columns are the pristine Interplanetary Magnetic Field, solar wind particle density and bulk velocity. The plasma beta has been kept fixed to $\beta = 0.4$ for all the simulations.

work characterized by a 2D planar shock front geometry, the bow-shock nominal surface cannot be directly inferred due to its 3D-curved shape. In fact, we face two difficulties: (i) the identification of a 3D oscillating curved surface, and (ii) the estimation of a 3D undisturbed nominal surface along which the ripples are generated. As such, to identify a representative bow-shock nominal surface, we proceeded as follows (figure 2 gives an illustration of these steps over a cross-section along the magnetic equatorial plane of the 3D outputs):

1. We use the *Z*-component of the current density as the best parameter to highlight the bow-shock boundary (e.g., (Lopez, 2018)), as shown in panels (a) and (c), where cross-sections of J_z in the magnetic equatorial plane *XY* and meridian plane *XZ* are illustrated (normalised to the upstream reference value).

2. Thanks to the structured nature of computer simulation outputs, we screen out the values along the *X* coordinate (for each specific *Y* and *Z* coordinate of the input plane) until a specific threshold based on the quantity defined in the previous step is met. Similarly to a binary approach, whenever the condition is met, that particular position's value is flipped from a background value of 0 to the arbitrarily value of 1, the screening is stopped and the following coordinate is considered. As a result, all the grid points marked with such value 1 describe a 3D pixeled map of the bow-shock boundary. Panels (b) and (d) represent its cross-sections in the magnetic equatorial plane *XY* and meridian plane *XZ*.

3. We use a linear regression method tool to fit the 3D pixeled map to find the coefficients of a 3D paraboloid surface (given by Equation 1), which can

now be considered as the undisturbed nominal bow-shock surface (a similar fitting technique has been used in the past to describe the bow-shock shape from observations, e.g., Formisano (1979)). The purple curves superimposed in Panels 2b and 2d show a cross-section of this nominal 3D paraboloid surface.

$$\gamma(y, z) = x(y, z) = a_{2,0}y^2 + a_{1,1}yz + a_{0,2}z^2 + a_{1,0}y + a_{0,1}z + a_{0,0} \quad (1)$$

We tested the accuracy of Equation 1 by evaluating the distance ($BS_{nom} - BS_{real}$) averaged over 50 ω_{ci}^{-1} between the fitted 3D nominal shock surface (BS_{nom}) and the detected real shock surface (BS_{real}). Figure 3 shows its values in the magnetic equatorial plane XY and meridian plane XZ. The x-axis quantity d_{BS} represents the distance from a point to the bow-shock at $(Y, Z) = (0, 0)$ d_i along the surface. A positive value indicates that the position of the fitted nominal surface is more sunward than the position of the real detected surface, whereas a negative value indicates the opposite site. From this plot, we observe that: (i) a maximum loss of accuracy of ≤ 2 d_i occurs at the nose, (ii) it is reduced to less than 1 d_i at the flanks, and (iii) it is limited to less than $0.25 - 0.30$ d_i elsewhere, which shows the validity of this technique in finding an accurate description of the shock nominal surface.

4 Results

4.1 3D Ripples Dynamics

We have applied the technique explained in the previous section to the $300 \leq t \leq 400$ ω_{ci}^{-1} simulation time range with an interval of $\Delta t_s = 0.5$ ω_{ci}^{-1}. The results are shown in the upper panels of Figure 4, which represent a 2D projected view of the 3D bow-shock surface at three different times. Similar to what was represented earlier, the map coordinates $d_{BS,y}$ and $d_{BS,z}$ correspond to the distance to the bow-shock nose along the curved surface, respectively, in the Y and Z directions. The plotted quantity is the magnetic field intensity normalised to the upstream IMF value. Given the chosen colormap, any signature other than blue corresponds to an increase in the magnetic intensity value, to indicate that the nominal surface is crossing the region downstream of the shock front (i.e., magnetosheath region), thus representing the occurrence of a ripple crossing.

From the maps in Figure 4, we can observe the following:

- In the high M_A regime (upper panels), the nominal surface is crossed by an intense rippling. The global dynamics show that the ripples behave like
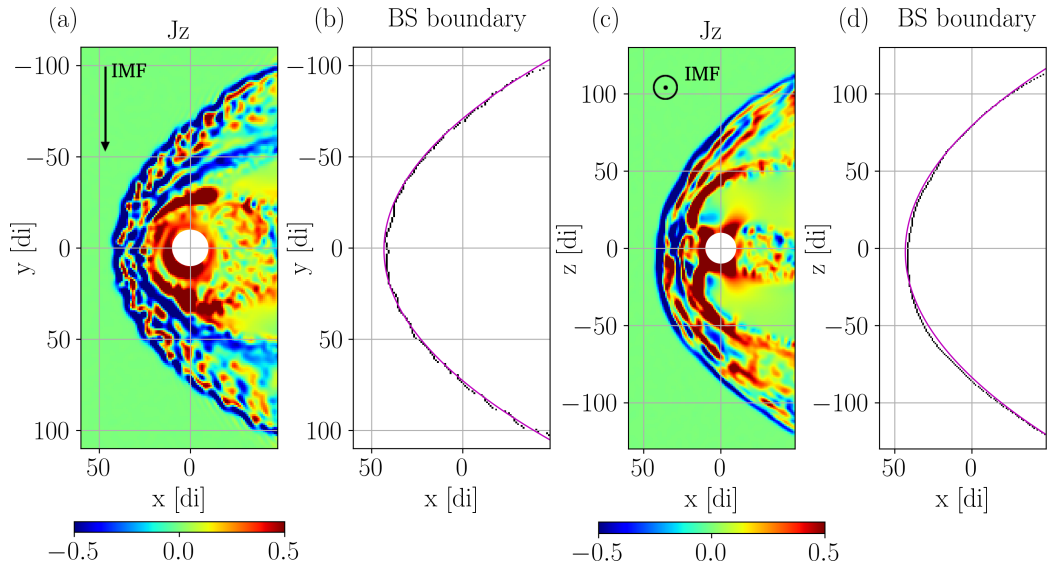
8

Figure 2: Illustration of the technique used to determine the bow-shock nominal surface from a 3D simulation output, as explained in the text. Panels (a) and (c): cross-sections along the magnetic equatorial plane at $Z = 0$ d_i and meridian plane at $Y = 0$ d_i of the 3D current density Z-component, which well highlights the bow-shock boundary compared to the background value. The arrows indicate the IMF direction with respect to these planes. Panels (b) and (d) show the 3D cross-section of the detected bow-shock boundary (black profile) and of the fitted bow-shock nominal surface (purple profile).
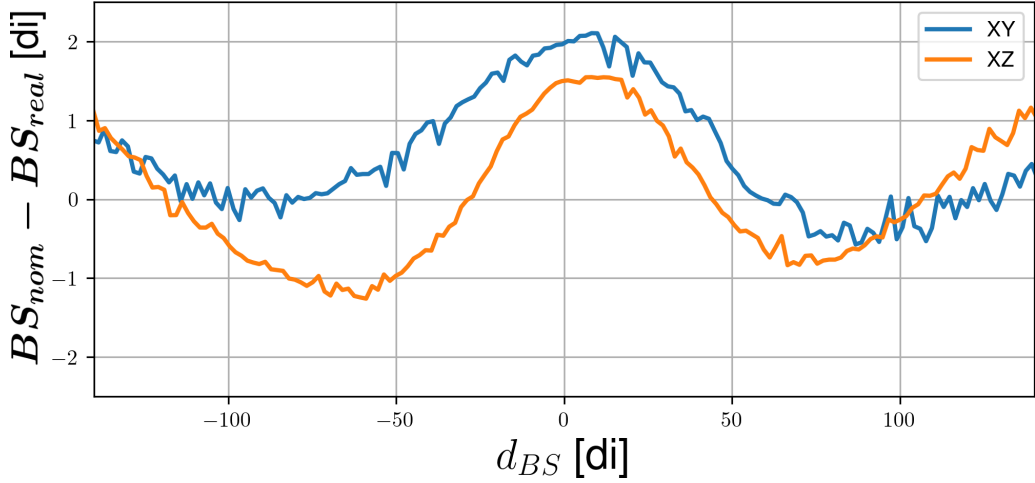
Figure 3: Profile of accuracy of the fitting model as computed with the normal-aligned time-averaged distance between the fitted nominal surface (BS_{nom}) and the real detected surface (BS_{real}) across two indicative planes: the magnetic equatorial plane *XY* and meridian plane *XZ*. Values averaged over $50\omega ci^{-1}$. The x-axis value d_{BS} represents the real distance along the nominal surface to the bow-shock nose at $(Y, Z) = (0, 0)$.

single elongated structures extending nearly as long as the entire North-South-range and moving consistently east (west)-ward along the flanks. We have highlighted the propagation of one of these structures with a dashed line as reference. The whole outcome is also available in the form of an animation in the supplemental material, which gives better insight into the global azimuthal propagation along the flanks.

- We do not observe any noticeable rippling signature around the nose area nor on the flanks near the external boundary. Such absence is due to the fact that, in these regions, there is a discrepancy between the nominal and the detected surface, as shown in Figure 3, so that Equation 1 is not able to accurately detect all the details of the bow-shock shape. Nevertheless, the presence of ripples in these regions can be confirmed by slightly shifting the nominal surface along the *X*-axis, as shown in the zoom map of the nose region in Figure 4 (holding the same colorscale as the upper panels).

- The vertical configuration of ripples and their azimuthal propagation depends on the specific magnetic field orientation along the *Y* coordinate. In order to corroborate such B-oriented propagation behaviour, we simulated a quasiperpendicular scenario with the IMF oriented along the *Z* coordinate (results not shown here), which showed similar structures propagating from

the nose region outwards toward the bow-shock poles along the magnetic field orientation.

- We do not observe any noticeable difference between the dynamics in the two flanks.

- For sake of comparison, we have plotted the results from applying the same technique on a low Alfvénic Mach number quasiperpendicular scenario with $M_A = 3.87$, which shows that rippling does not occur at low Alfvénic Mach numbers (for this case, the colorscale has been further saturated for better visualisation).

4.2 Ripples Dynamics Properties

Given the homogeneous north–south elongated geometry held by ripples and the fact that they are propagating flank-wards, we can provide more insights into their dynamics by reducing the global 3D problem to an azimuthal analysis by applying the same technique used in the previous section on a selected XY plane. Considering a cross-section along the magnetic equatorial plane (i.e., at $Z = 0.0\ d_i$), we obtain the temporal evolution map shown in Panel (a) of Figure 5 (hereafter named 5a). The abscissa represents the distance of a point of the bow-shock to the nose at $(Y, Z) = (0, 0)$ along the bow-shock. We will refer to the regions from $d_{BS}^- \leq d_{BS} \leq 0$ as left wing and the regions $0 \geq d_{BS} \geq d_{BS}^+$ as right wing, where d_{BS}^- and d_{BS}^+ indicate the farthest points on the left and right sides with respect to the bow-shock nose at $d_{BS} = 0$. The region where $\theta_{\mathbf{B}\hat{\mathbf{n}}} \sim 45°$ lies at $d_{BS} \sim \pm 68\ d_i$. The vertical axis represents the time range when the steady-state conditions are reached, between 300 and 400 ω_{ci}^{-1}. The represented quantity is again the magnetic field intensity normalised to the upstream IMF value: an increase in the colorscale (yellow-reddish) indicates that the nominal surface intercepts the highly magnetic field in the region behind the shock front, while a more blueish colour indicates that the nominal surface is intercepting the upstream IMF.

From Figure 5, we can infer the following:

- Overall, we do not observe any significant difference in the ripple propagation between the two wings.

- The locations of the ripples mainly form straight lines nearly parallel to each other in time, indicating an approximately constant propagation velocity along the surface (Panel 5a). The slope of those lines gives an approximate ripple propagation velocity estimation in the range $7 - 9\ V_A$ (V_A being the upstream Alfvén speed).
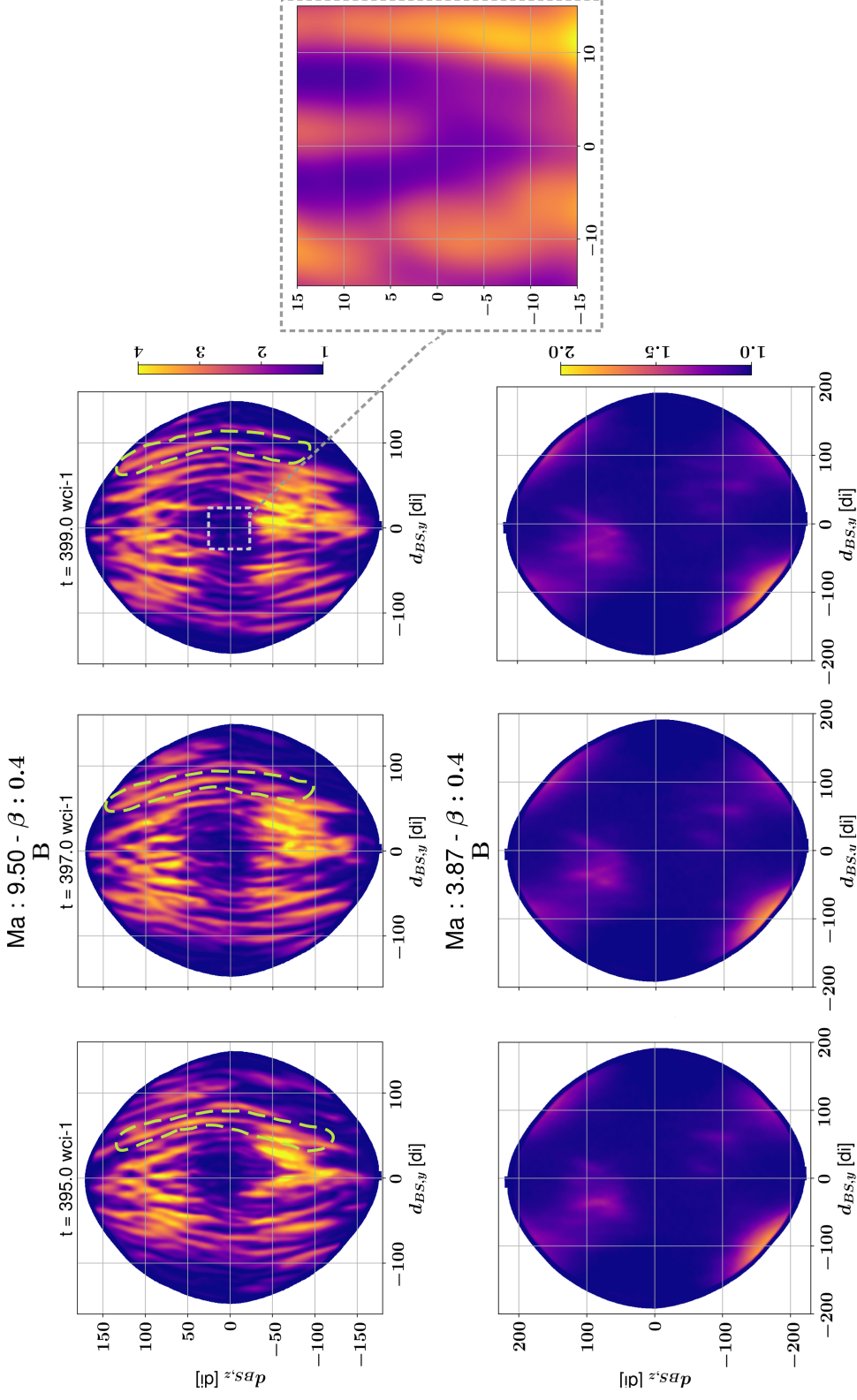
11

Figure 4: Maps of the magnetic field intensity normalised to the upstream IMF value along the nominal bow-shock surface. Upper panels: situation at high Alfvénic Mach number $M_A = 9.5$. A zoom-in of the nose region is given in the aside window (same colorscale). Lower panels: situation at lower Mach number $M_A = 3.8$ ($\beta = 0.4$). The axes represent the real distance between of a point of the bow-shock surface, in upstream ion skin depths d_i, to the nose at $(d_{BS,y}, d_{BS,z}) = (0, 0)$ d_i.

Additionally, we performed a fast Fourier transform (FFT) spectral analysis of the map in Panel (5a) to derive the frequency-wavelength dispersion relations shown in Panel (5b). A Gaussian filter has been applied to the input data to remove noisy frequencies for a more readable plot. Similarly to what done in Lowe and Burgess (2003), the space-time nonperiodicity has been fixed by applying a Hann window function (e.g., Press et al., 1988) to both space and time directions to reduce the spectrum leakage. This function is commonly used in signal processing to force the signal periodicity for a correct application of the FFT. It consists in giving the signal components a weight factor w based on a cosine distribution as $w(n) = 0.5 - 0.5 \cos\left(\frac{2\pi n}{M-1}\right)$, where $0 \le n \le M - 1$ is the n_{th} sample of a vector with a size of M (M corresponds to the window's size). In this specific 2D case, this window has been applied recursively to each row and each column of the map in Figure (5a) as described in Pielawski and Wählby (2020). After applying the Hann window, we performed a 2D FFT to obtain the spectrum in Figure (5b). We should remark that the overall spectrum is actually the composition of two different signals representing each single bow-shock wing: the signal into the negative domain represents the rippling evolution along the right wing ($0 \le d_{BS} \le d_{BS}^+ \ d_i$), whereas that in the positive domain represents the evolution along the left wing ($d_{BS}^- \le d_{BS} \le 0 \ d_i$).

This panel shows the following:

- The spectrum is nearly symmetric over the two wings, as expected given the highly symmetric configuration of this scenario. In particular, the spectrum shows the presence of a dominant linear signal covering a range of wavelengths $\ge 8.0 \ d_i$, limited here by the sampling Nyquist frequency, which is in line with the values found from past planar shock-front simulations (Winske and Quest, 1988; Lowe and Burgess, 2003; Burgess and Scholer, 2007; Yuan et al., 2009). At low frequencies, we observe other signatures covering a broader band.

- The slope of the spectrum signal in both wings gives ripple propagation velocity of ~ 8 times the upstream Alfvén speed V_A. We can compare this value with the local magnetic equatorial solar wind average tangential velocity (the bow-shock nominal surface does not change shape over time, so the surface locations on the map in Panel (5a) are not dependent on time). This velocity is evaluated upon retrieving the 2D nominal surface information along the magnetic equatorial plane with the technique explained earlier and considering that the solar wind bulk velocity flows mainly in the X-direction by neglecting the out-of-plane components. We found an average tangential velocity of $\sim 6.6 \ V_A$, nearly $\sim 1.5 \ V_A$ lower than the ripples propagation velocity. Such a discrepancy may be due to the fact
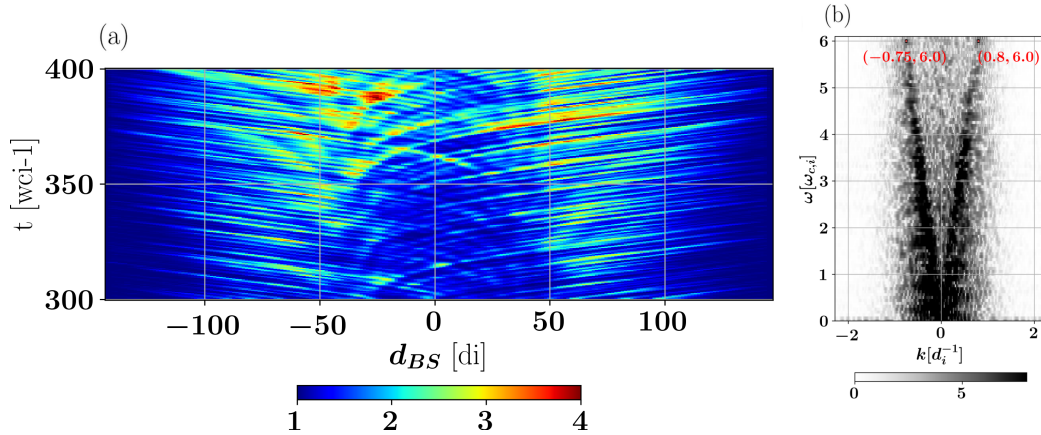
Figure 5: Panel (a): space-time map of the bow-shock surface dynamics across the nominal surface detected for the magnetic equatorial plane at $Z = 0$ d_i. The abscissa represents the real distance of a point of the bow-shock surface, in upstream ion skin depths d_i, to the nose at ($d_{BS} = 0$ d_i), whereas the y-axis represents the time range considered upon the steady-state conditions are achieved. Panel (b): Fast Fourier spectral analysis of the map in Panel (a).

that these values are normalised to the Alfvén speed evaluated with the upstream magnetic field and density values. By considering the magnetic field and density values, e.g., at the bow-shock overshoot, as done in Lowe and Burgess (2003), we obtain a local Alfvén speed of $V_{A,o} \sim 3-4$ V_A, yielding ripples propagation velocity more in line with the local tangential velocity found here.

- Finally, by performing the same 2D analysis at different latitudes, we found that ripples propagate slightly slower (e.g., on the plane at $Z \pm 75.0$ d_i the ripples speed is observed to be ~ 6.5 V_A - plots not shown here). However, this last value is affected by the global 3D geometrical configuration: because the bow-shock shape is a paraboloid, velocities towards the poles are seen to be smaller than that at the equator. Thanks to the representation adopted in the maps in Figure 4, we can directly compare the propagation distance at a specific latitude with that at the equator (i.e., at $Z = 0$ d_i), finding a constant ratio in line with the ratio between the average velocities. This confirms that ripples are indeed propagating from the magnetic noon meridian outwards along the bow-shock surface at a constant speed as single elongated structures throughout the latitudes.

4.3 Bow-shock Nose Region and Shock-Front Reformation Occurrence

From Figures 4 and 5, we could infer that ripples propagate from noon meridian to the flanks of the bow-shock. Hence, we decided to better investigate the noon meridian region around the subsolar point. Given the global bow-shock size, this region can be approximated as a planar shock front in quasiperpendicular configuration. One of the possible mechanisms thought to be responsible for shock-surface rippling in planar shock geometry is shock-front reformation. Indeed, shock-front reformation is a highly nonstationary kinetic phenomenon occurring in high Alfvénic Mach number quasiperpendicular collisionless shocks. Such a hypothesis is also supported by our results in figure 4, which evidenced no rippling in the low M_A case.

In particular, supercritical collisionless shock fronts in relative motion with a constant flux of charged particles are able to reflect a certain amount of the incoming particles, which are responsible for the creation of the shock foot structure. The rest of the particles are directly transmitted downstream.

Shock-front reformation occurs when the number of reflected ions at the shock front is high enough to begin accumulating in front of it by generating a new growing foot region that will eventually result in a new ramp replacing the old one, thus creating a new shock-front.

Shock-reformation in quasiperpendicular shocks has been studied with full kinetic and hybrid simulations in 1D and 2D planar shock configurations (Lembege and Savoini, 1992; Hellinger et al., 2002; Hada et al., 2003; Yang et al., 2009a,b, 2011b,a; Lembège et al., 2009; Yuan et al., 2009). Specifically, Hellinger et al. (2002) found that this process can only occur for low values of plasma β and high Alfénic Mach numbers. Moreover, shock-front reformation is expected to be observed with a more refined resolution than the ion gyroscale, with the shock front appearing stationary otherwise (Hellinger et al., 2002; Yang et al., 2009b; Lembège et al., 2009; Yuan et al., 2009).

Signatures of Shock-Front Reformation at the Bow-Shock Nose

With an IMF strictly perpendicular to the normal direction and a solar wind flow nearly perfectly aligned to it, the bow-shock nose is the region of maximum energy conversion between the incoming solar wind and the geomagnetic system. To gain better insights into the dynamics occurring in this particular region, we ran a highly resolved simulation of the same $M_A = 9.50$ scenario by significantly increasing the spatial resolution in the XY plane, while keeping a coarse resolution in Z to limit the computational costs. As pointed out in Section 2.1, the new space-time resolution is now $\Delta x = \Delta y = 0.2\,d_i$ and $\Delta t = 5\cdot10^{-4}\,\omega_{ci}^{-1} \sim 8.4\cdot10^{-4}\,s$.

In particular, we analysed the phase space density in the local magnetic field frame of reference across the bow-shock nose along its normal direction within a $\pm 2 \times \pm 2 \times 14 d_i$ domain box, as shown in Figure 6. The abscissa represents the GSE X-coordinate, while $V_{\hat{\mathbf{n}}}$ represents the velocity perpendicular to the local magnetic field projected on the nominal bow-shock surface normal direction. The representation in the top panel shows the reflection process which some particles undergo as the solar wind approaches the bow-shock front: the solar wind flows undisturbed with a steady velocity of $\sim -10 \, V_A$ until approximately $X \sim 38 \, d_i$, where particles begin to decelerate (i.e., $V_{\hat{\mathbf{n}}}$ passes from $-10 \, V_A$ to $\sim +5 \, V_A$) and be reflected (i.e., GSE X-position passes from $X \sim 38 \, d_i$ to $\sim 36 - 37 \, d_i$ and back to $\sim 38 - 40 \, d_i$), forming the typical reflected particle loop shape. Additionally, we can observe that a consistent number of particles are transmitted downstream with a velocity $-7 \, V_A < V_{\hat{\mathbf{n}}} < 3 \, V_A$ by increasing their thermal velocity.

To better highlight the complex dynamics at the nose region, in the rest of the panels in Figure 6, we have plotted the difference between the phase-space at two consecutive time steps. Hence, each panel represents the difference between the particle space velocity at time step t_{i+1} minus the old time step t_i (e.g., the second panel shows the difference between $t = 90.2 \, \omega_{ci}^{-1}$ and $t = 90.0 \, \omega_{ci}^{-1}$). All the plotting features, such as axis limits, number of bins and domain volume, have been kept constant to give an insight into the effective dynamics. The negative/positive values have been maintained to highlight those regions being either filled or depleted of particles with respect to the previous time step. In particular, we refer to particle-added (particle-depleted) clusters as those regions showing an addition (depletion) of particles. Given the chosen colormap, particle-added regions will appear red, whereas particle-depleted regions will appear blue. From this representation, we observe the following:

- A red-coloured particle-added cluster is seen rotating along the loop's trajectory to indicate a moving time-dependent surplus of reflected particles (dynamics highlighted in the figure with a dashed arrow). At each time step, this cluster increases the number of particles in that phase-space region with respect to the previous time frame. In particular, at time $90.2 \, \omega_{ci}^{-1}$, this cluster shows a global positive velocity and a location in the proximity of the shock-front position ($X \sim 37 \, d_i$) to indicate an increased number of particles directly departing from the shock-front with respect to the previous time step. As time goes on, this cluster rotates to the phase-space region of velocity $V_{\hat{\mathbf{n}}} \sim 0 \, V_A$ at time $90.4 \, \omega_{ci}^{-1}$, of a negative velocity $V_{\hat{\mathbf{n}}} < 0$ at time $90.6 \, \omega_{ci}^{-1}$ and of an even more negative velocity at time $90.8 \, \omega_{ci}^{-1}$. Then, we observed the cluster to merge with the foot at time $91.0 \, \omega_{ci}^{-1}$ and disappear at $91.2 \, \omega_{ci}^{-1}$. At this latter time, the loop is closed, and the cycle of shock-front reformation is terminated. Such a time interval, i.e., $\sim 1.2 \, \omega_{ci}^{-1}$ in terms

of upstream normalised value, corresponds to the characteristic shock-front reformation cycle period in this specific scenario.

- The foot region appears to be very dynamic: from the phase-space difference map at $90.2 < t < 90.8\ \omega_{ci}^{-1}$, we can observe the formation and growth of a red-coloured particle-added cluster above a blue-coloured particle-depleted cluster. This is a signature of foot growth due to particle accumulation, the generation of a secondary foot due to an increase in the magnetic field intensity and the formation of a new ramp.

Additionally, we plotted in Figure 7 a space-time evolution map of the magnetic field intensity across the bow-shock nose. The x-axis represents the spatial *X*-position of the line cut across the nose, where the y-axis represents the time range. The magnetic field is normalised to the upstream value. From this map, we can observe the following:

- The magnetic field shows the typical foot-ramp-overshoot structure of collisionless supercritical shocks under a quasiperpendicular interaction. Based on the figure colormap, the foot region is highlighted in light blue, the ramp in yellow and the overshoot immediately following the ramp in red. In particular, we will consider the mid-ramp point at $\frac{B}{B_0} = 4$ as reference for the shock front. With respect to the mid-ramp point, we identified three different types of displacement: (i) the magnetic field shows a global forward motion (i.e., an expansion with respect to the Earth-Sun line) between $90.0 < t < 90.4$ with a displacement of $\sim 0.5\ d_i$, followed by a (ii) backward motion (i.e., a contraction with respect to the Earth-Sun line) between $90.4 < t < 91.2$ with a displacement of $\sim 1.0 - 1.5\ d_i$, and (iii) a further forward motion afterwards between $91.4 < t < 92.0$ with a displacement of $\sim 0.5\ d_i$. The profiles at $t = 90.4\ \omega_{ci}^{-1}$ and $t = 91.2/91.4\ \omega_{ci}^{-1}$ represent the extreme profile positions observed. The forward motion can be explained with the shock-front reformation process generating a new foot-ramp structure, while the backward motion can be explained by the counterpush undergone by the shock front to restore the bow-shock equilibrium conditions with pristine solar wind.

- We observe the presence of a variable foot region: this is highlighted by the green signature in the map, which indicates the presence of a sort of dynamical plateau between the ramp and the solar wind. This can be interpreted as an indication of shock-front reformation occurrence: particles accumulate in the foot region by growing and generating the plateau, which subsequently begins to act as a new shock ramp and reflects the incoming
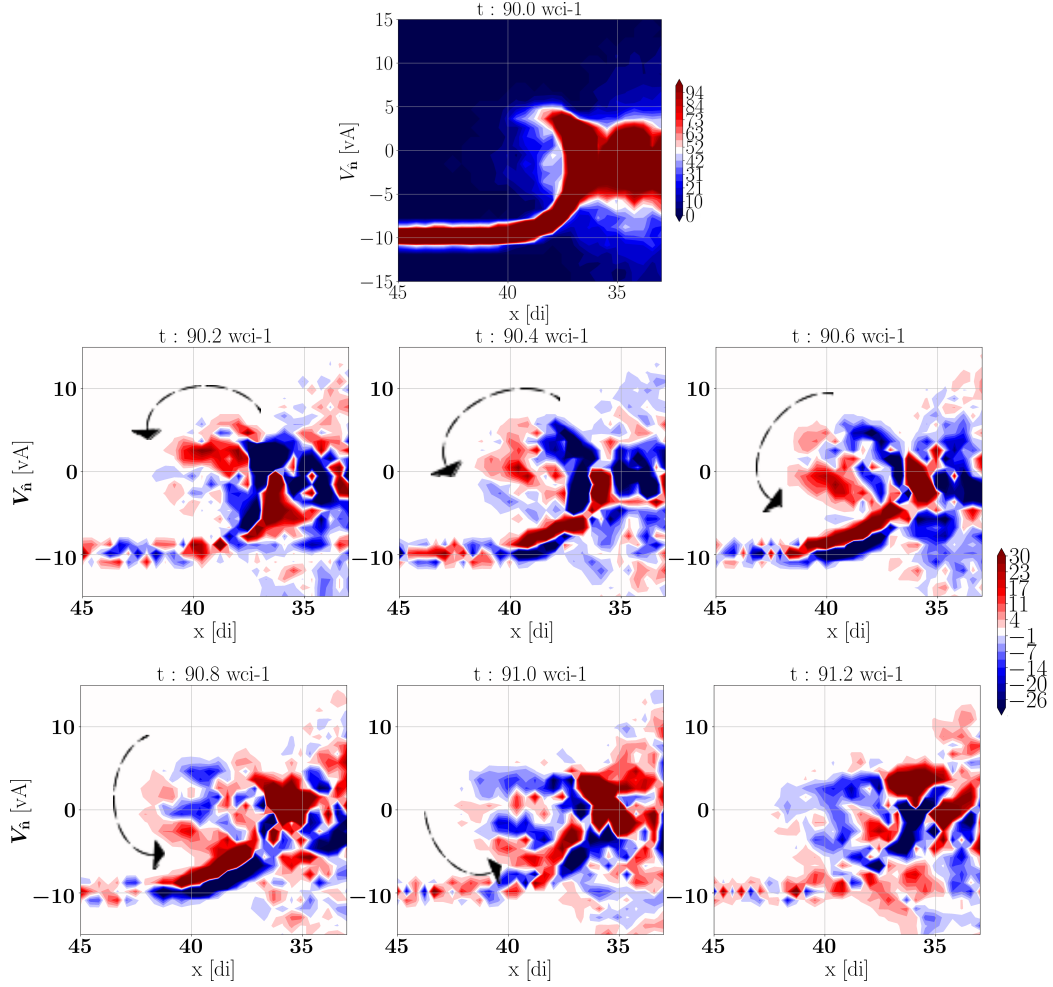
17

Figure 6: Set of maps representing the particles phase-space in the $X - V_{\hat{\mathbf{n}}}$ domain, $V_{\hat{\mathbf{n}}}$ being the velocity component as explained in the text, normalised to the upstream Alfvén speed V_A, and X is the space distance normalised to the upstream ion skin depth d_i. The colour bar represents the number of (computational)-particles per phase-space volume. The first panel at $t = 90.0\ \omega_{ci}^{-1}$ represents the entire phase space, from which we can distinguish the density of the particles reflected by the supercritical shock-front, as well as the density of the particles ultimately being transmitted downstream. All the other panels represent the difference between the phase space at that specific time and the previous time frame. The dashed arrow indicates the temporal rotating motion of the red cluster as a signature of ongoing shock-front reformation.

18

particles, so that a new foot region before it is expected to form. Furthermore, new particles are still being reflected back and accumulated by this moving ramp (which is the new shock-front) by leading to the foot region growth even if the ramp is moving backwards.

Hence, an analysis of the ion phase-space and the magnetic field space-time evolution across the bow-shock nose revealed the occurrence of an intense shock-front reformation in this region.

5   Discussion and Conclusions

The study of collisionless shock-front rippling in the quasiperpendicular regime has long been studied with numerical simulations over the past decades for 1D and 2D planar shocks. In this work, we proposed an analysis of the global bow-shock dynamics under the quasiperpendicular condition in the still poorly covered 3D curved scenario. In particular, we performed 3D hybrid simulations to give new insights into the 3D rippling behaviour of an Earth-like curved bow-shock as a result of a system nonstationarity upon a quasiperpendicular interaction with the IMF. The quasiperpendicularity is set by considering an IMF direction whose components only lie along the GSE Y coordinate. The novelty of such a scenario consists in a realistic evolution of a quasiperpendicular interaction at the nose region into an oblique scenario as we move along the flanks within the same connected global system. Moreover, unlike the scenarios studied with ad hoc planar slabs, here the interaction between the bulk solar wind velocity and the shock front passes from a perfectly perpendicular regime $\theta_{\mathbf{V}\hat{\mathbf{n}}} = 0°$ toward a more unusual and poorly studied oblique $\theta_{\mathbf{V}\hat{\mathbf{n}}} = 60°$ interaction at the flanks.

In particular, the study of propagating ripples along a curved surface in the 3D space added some complexity in the analysis related to (i) the identification of a wavy curved bow-shock surface and (ii) the 3D estimation of an undisturbed nominal surface. We found that using a 3D-paraboloid model provided a good estimate of the shock surface.

First, we have noticed that the ripples are present for a relatively high Alfvénic Mach number, while absent for low Alfvénic Mach numbers, as already found in past studies (Hellinger and Mangeney, 1997). We have also discovered that they indeed hold the shape of elongated structures extending along the magnetic noon meridian for almost the entire North–South range perpendicular to **B**. Additionally, they are seen to propagate parallel to the IMF orientation with a constant velocity from the noon meridian towards the respective flanks at $+Y$ and $-Y$, without any noticeable difference in their dynamics between the two directions. To our knowledge, the latter behaviour was never observed or specifically analysed
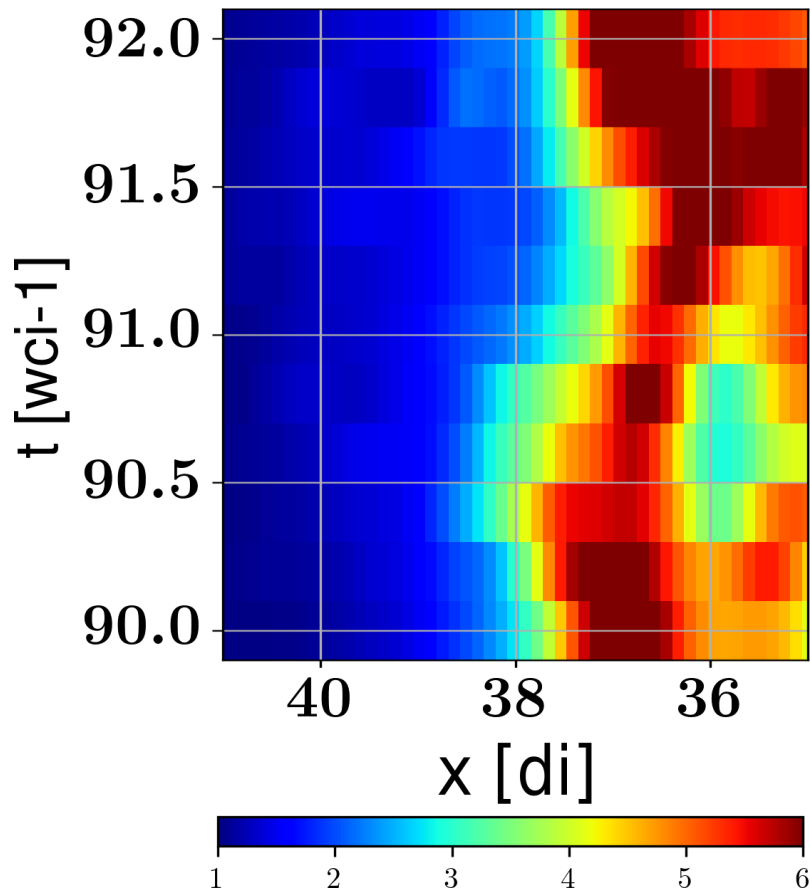
Figure 7: Space-time map of the magnetic field intensity evolution across the bow-shock nose. The x-axis represents the *X* component of the line cut (in GSE coordinates, expressed in upstream ion skin depth d_i), while the y-axis represents the time range considered (expressed in upstream ion gyroperiod). Magnetic field values normalised to the upstream IMF value.

before and could be explained by the symmetric configuration held by the system with respect to the solar wind inflow. In fact, past analyses of planar shocks subjected to solar wind flow perpendicular to the surface pointed out that ripples propagate towards a specific direction depending on the upstream magnetic field. For instance, Lowe and Burgess (2003) found that, when the upstream magnetic field is parallel to the shock front, the ripples propagate in the same direction as that defined by the upstream magnetic field. In a later paper, Burgess and Scholer (2007) analysed the case of a quasiperpendicular interaction with the upstream magnetic field directed along the out-of-plane direction; after reversing the magnetic field direction, the ripples still propagated parallel to the shock-front but they inverted their sense of propagation.

In our case of a 3D curved shock, the ripples propagate toward both flanks. This suggests that, in a 3D curved scenario, the component of the solar wind tangential velocity lying on the IMF plane plays an important role in the ripples' propagation. For instance, in the case analysed here, the solar wind tangential components in the magnetic equatorial plane XY containing the IMF direction appear to affect the ripple propagation direction. To corroborate this hypothesis, we have simulated the same scenario with a flipped IMF direction: with $\theta_{\mathbf{B}\hat{\mathbf{n}}} = 90°$ at the nose and the IMF oriented along Z (results not shown here), finding that the ripples are now elongated structures extending in the azimuthal direction and propagating along the Z direction, i.e., parallel to the upstream IMF direction and following the tangential component of the solar wind that belongs to the YZ plane containing the IMF.

An FFT analysis provided an estimate of the velocity on the order of nearly 8 times the upstream solar wind Alfvén speed and showed a broad range of wavelengths greater than 8 d_i. These results are in line with those found with different past ad hoc slab shock-fronts simulations and satellite observations (e.g., Lowe and Burgess (2003); Johlander et al. (2016)). On the other hand, this value is not restrictive and smaller wavelengths are also expected, provided that the detection tool features a sufficient sampling resolution.

In a quasiperpendicular configuration, the ripple source has long been debated and still not completely understood due to the possible synergy between MHD and kinetic scales. However, although their propagation can be explained with MHD surface waves, an intrinsic kinetic trigger mechanism is still likely to be the effective source. The fact that ripples appear to propagate from the noon meridian region and that they expand symmetrically outwards along the flank directions suggests that the possible kinetic trigger mechanism should lie along the shock normal rather than along the magnetic field direction. Given our quasiperpendicular configuration, we investigated for the possible occurrence of the shock-front reformation process. Even though signatures of shock-front reformation could already be seen with the resolution proposed for the global dynamics analysis, we

consolidated this hypothesis by running the same setup with a much higher space resolution in the XY plane ($\Delta x = \Delta y = 0.2\ d_i$, $\Delta z = 4\ d_i$). An analysis of the ion velocity distribution and of the temporal magnetic field intensity evolution profile across the bow-shock nose revealed that an intense shock-front reformation is actually taking place in this region. Moreover, this process was not observed in the same configuration in the low Alfvénic Mach number case, corroborating the fact that shock-front reformation and bow-shock rippling can be directly related. In particular, the simultaneous presence of these two phenomena, i.e., shock-front reformation and rippling, suggests the following possible mechanism: the kinetic process of shock-front reformation perturbs the system locally within a restricted region as the bow shock nose, generating an inward and outward displacement of the shock surface. The forward motion is driven by the shock-front reformation process generating a new foot-ramp structure, while the backward motion is driven by the re-establishment of the equilibrium conditions between pristine solar wind and bow-shock boundary. This motion in turn induces a modulation that later propagates as an MHD surface wave along the bow-shock boundary. The analysis performed here does not exclude that other kinetic processes may play a role in rippling generation. Nevertheless, we identified that shock-front reformation at the nose is a good candidate to explain the rippling of the bow-shock surface.

Acknowledgements

References

Aizawa, S., Persson, M., Menez, T., André, N., Modolo, R., Génot, V., Sanchez-Cano, B., Volwerk, M., Chaufray, J.Y., Baskevitch, C., Heyner, D., Saito, Y., Harada, Y., Leblanc, F., Barthe, A., Penou, E., Fedorov, A., Sauvaud, J.A., Yokota, S., Auster, U., Richter, I., Mieth, J., Horbury, T.S., Louarn, P., Owen, C.J., Murakami, G., 2022. LatHyS global hybrid simulation of the Bepi-Colombo second Venus flyby. 218, 105499. doi:10.1016/j.pss.2022.105499.

Burgess, D., Scholer, M., 2007. Shock front instability associated with reflected ions at the perpendicular shock. Physics of Plasmas 14, 012108–012108. doi:10.1063/1.2435317.

Formisano, V., 1979. Orientation and Shape of the Earth's Bow Shock in Three Dimensions. 27, 1151–1161. doi:10.1016/0032-0633(79)90135-1.

Hada, T., Oonishi, M., LembèGe, B., Savoini, P., 2003. Shock front nonstationarity of supercritical perpendicular shocks. Journal of Geophysical Research (Space Physics) 108, 1233. doi:10.1029/2002JA009339.

Hellinger, P., Mangeney, A., 1997. Upstream whistlers generated by protons reflected from a quasi-perpendicular shock. 102, 9809–9820. doi:10.1029/96JA03826.

Hellinger, P., Mangeney, A., Matthews, A., 1996. Whistler waves in 3D hybrid simulations of quasiperpendicular shocks. 23, 621–624. doi:10.1029/96GL00453.

Hellinger, P., Trávnícek, P., Matsumoto, H., 2002. Reformation of perpendicular shocks: Hybrid simulations. 29, 2234. doi:10.1029/2002GL015915.

Jeřáb, M., Němeček, Z., Šafránková, J., Jelínek, K., Měrka, J., 2005. Improved bow shock model with dependence on the IMF strength. 53, 85–93. doi:10.1016/j.pss.2004.09.032.

Johlander, A., Schwartz, S.J., Vaivads, A., Khotyaintsev, Y.V., Gingell, I., Peng, I.B., Markidis, S., Lindqvist, P.A., Ergun, R.E., Marklund, G.T., Plaschke, F., Magnes, W., Strangeway, R.J., Russell, C.T., Wei, H., Torbert, R.B., Paterson, W.R., Gershman, D.J., Dorelli, J.C., Avanov, L.A., Lavraud, B., Saito, Y., Giles, B.L., Pollock, C.J., Burch, J.L., 2016. Rippled Quasiperpendicular Shock Observed by the Magnetospheric Multiscale Spacecraft. 117, 165101. doi:10.1103/PhysRevLett.117.165101.

Karimabadi, H., Roytershteyn, V., Vu, H.X., Omelchenko, Y.A., Scudder, J., Daughton, W., Dimmock, A., Nykyri, K., Wan, M., Sibeck, D., Tatineni, M., Majumdar, A., Loring, B., Geveci, B., 2014. The link between shocks, turbulence, and magnetic reconnection in collisionless plasmas. Physics of Plasmas 21, 062308. doi:10.1063/1.4882875.

Kotova, G., Verigin, M., Gombosi, T., Kabin, K., Slavin, J., Bezrukikh, V., 2021. Physics-based analytical model of the planetary bow shock position and shape. Journal of Geophysical Research: Space Physics 126, e2021JA029104.

Krasnoselskikh, V.V., Lembège, B., Savoini, P., Lobzin, V.V., 2002. Nonstationarity of strong collisionless quasiperpendicular shocks: Theory and full particle numerical simulations. Physics of Plasmas 9, 1192–1209. doi:10.1063/1.1457465.

Krauss-Varban, D., Li, Y., Luhmann, J.G., 2008. Ion acceleration at the earth's bow shock and at interplanetary shocks: A comparison, in: AIP Conference Proceedings, American Institute of Physics. pp. 307–313. doi:10.1063/1.2982463.

Lembege, B., Savoini, P., 1992. Nonstationarity of a two-dimensional quasiperpendicular supercritical collisionless shock by self-reformation. Physics of Fluids B 4, 3533–3548. doi:10.1063/1.860361.

Lembège, B., Savoini, P., Hellinger, P., Trávníček, P.M., 2009. Nonstationarity of a two-dimensional perpendicular shock: Competing mechanisms. Journal of Geophysical Research (Space Physics) 114, A03217. doi:10.1029/2008JA013618.

Lobzin, V.V., Krasnoselskikh, V.V., Bosqued, J.M., Pinçon, J.L., Schwartz, S.J., Dunlop, M., 2007. Nonstationarity and reformation of high-Mach-number quasiperpendicular shocks: Cluster observations. 34, L05107. doi:10.1029/2006GL029095.

Lopez, R.E., 2018. The Bow Shock Current System, in: Keiling, A., Marghitu, O., Wheatland, M. (Eds.), Electric Currents in Geospace and Beyond, pp. 477–496. doi:10.1002/9781119324522.ch28.

Lowe, R.E., Burgess, D., 2003. The properties and causes of rippling in quasi-perpendicular collisionless shock fronts. Annales Geophysicae 21, 671–679. doi:10.5194/angeo-21-671-2003.

Madanian, H., Desai, M.I., Schwartz, S.J., Wilson, L. B., I., Fuselier, S.A., Burch, J.L., Le Contel, O., Turner, D.L., Ogasawara, K., Brosius, A.L., Russell, C.T., Ergun, R.E., Ahmadi, N., Gershman, D.J., Lindqvist, P.A., 2021. The Dynamics of a High Mach Number Quasi-perpendicular Shock: MMS Observations. 908, 40. doi:10.3847/1538-4357/abcb88, arXiv:2011.12346.

Matthews, A.P., 1994. Current Advance Method and Cyclic Leapfrog for 2D Multispecies Hybrid Plasma Simulations. Journal of Computational Physics 112, 102–116. doi:10.1006/jcph.1994.1084.

Modolo, R., Chanteur, G.M., Dubinin, E., Matthews, A.P., 2005. Influence of the solar EUV flux on the Martian plasma environment. Annales Geophysicae 23, 433–444. doi:10.5194/angeo-23-433-2005.

Modolo, R., Hess, S., Mancini, M., Leblanc, F., Chaufray, J.Y., Brain, D., Leclercq, L., Esteban-Hernández, R., Chanteur, G., Weill, P., González-Galindo, F., Forget, F., Yagi, M., Mazelle, C., 2016. Mars-solar wind interaction: LatHyS, an improved parallel 3-D multispecies hybrid model. Journal of Geophysical Research (Space Physics) 121, 6378–6399. doi:10.1002/2015JA022324.

Moullard, O., Burgess, D., Horbury, T.S., Lucek, E.A., 2006. Ripples observed on the surface of the Earth's quasi-perpendicular bow shock. Journal of Geophysical Research (Space Physics) 111, A09113. doi:10.1029/2005JA011594.

Ofman, L., Gedalin, M., 2013. Rippled quasi-perpendicular collisionless shocks: Local and global normals. Journal of Geophysical Research (Space Physics) 118, 5999–6006. doi:10.1002/2013JA018780.

Omidi, N., Blanco-Cano, X., Russell, C., Karimabadi, H., 2004. Dipolar magnetospheres and their characterization as a function of magnetic moment. Advances in Space Research 33, 1996–2003. doi:10.1016/j.asr.2003.08.041.

Omidi, N., Desai, M., Russell, C.T., Howes, G.G., 2021. High Mach Number Quasi-Perpendicular Shocks: Spatial Versus Temporal Structure. Journal of Geophysical Research (Space Physics) 126, e29287. doi:10.1029/2021JA029287.

Pielawski, N., Wählby, C., 2020. Introducing hann windows for reducing edge-effects in patch-based image segmentation. PloS one 15, e0229839.

Press, W.H., Vetterling, W.T., Teukolsky, S.A., Flannery, B.P., 1988. Numerical recipes. Cambridge University Press.

Richer, E., Modolo, R., Chanteur, G.M., Hess, S., Leblanc, F., 2012. A global hybrid model for Mercury's interaction with the solar wind: Case study of the dipole representation. Journal of Geophysical Research (Space Physics) 117, A10228. doi:10.1029/2012JA017898.

Romanelli, N., Modolo, R., Leblanc, F., Chaufray, J.Y., Hess, S., Brain, D., Connerney, J., Halekas, J., Mcfadden, J., Jakosky, B., 2018. Effects of the Crustal Magnetic Fields and Changes in the IMF Orientation on the Magnetosphere of Mars: MAVEN Observations and LatHyS Results. Journal of Geophysical Research (Space Physics) 123, 5315–5333. doi:10.1029/2017JA025155.

Tanaka, M., Goodrich, C.C., Winske, D., Papadopoulos, K., 1983. A source of the backstreaming ion beams in the foreshock region. 88, 3046–3054. doi:10.1029/JA088iA04p03046.

Turc, L., Fontaine, D., Savoini, P., Modolo, R., 2015. 3D hybrid simulations of the interaction of a magnetic cloud with a bow shock. Journal of Geophysical Research (Space Physics) 120, 6133–6151. doi:10.1002/2015JA021318.

Wang, M., Lu, J., Kabin, K., Yuan, H., Zhou, Y., Guan, H., 2020. Influence of the interplanetary magnetic field cone angle on the geometry of bow shocks. The Astronomical Journal 159, 227.

Wang, M., Lu, J., Yuan, H., Kabin, K., Liu, Z.Q., Zhao, M., Li, G., 2015. The dipole tilt angle dependence of the bow shock for southward imf: Mhd results. Planetary and Space Science 106, 99–107.

Winske, D., Quest, K.B., 1988. Magnetic field and density fluctuations at perpendicular supercritical collisionless shocks. 93, 9681–9693. doi:10.1029/JA093iA09p09681.

Yang, Z.W., LembèGe, B., Lu, Q.M., 2011a. Acceleration of heavy ions by perpendicular collisionless shocks: Impact of the shock front nonstationarity. Journal of Geophysical Research (Space Physics) 116, A10202. doi:10.1029/2011JA016605.

Yang, Z.W., Lembège, B., Lu, Q.M., 2011b. Impact of the nonstationarity of a supercritical perpendicular collisionless shock on the dynamics and energy spectra of pickup ions. Journal of Geophysical Research (Space Physics) 116, A08216. doi:10.1029/2010JA016360.

Yang, Z.W., Lembège, B., Lu, Q.M., 2012. Impact of the rippling of a perpendicular shock front on ion dynamics. Journal of Geophysical Research (Space Physics) 117, A07222. doi:10.1029/2011JA017211.

Yang, Z.W., Lu, Q.M., Lembège, B., Wang, S., 2009a. Shock front nonstationarity and ion acceleration in supercritical perpendicular shocks. Journal of Geophysical Research (Space Physics) 114, A03111. doi:10.1029/2008JA013785.

Yang, Z.W., Lu, Q.M., Wang, S., 2009b. The evolution of the electric field at a nonstationary perpendicular shock. Physics of Plasmas 16, 124502. doi:10.1063/1.3275788.

Yuan, X., Cairns, I.H., Trichtchenko, L., Rankin, R., Danskin, D.W., 2009. Confirmation of quasi-perpendicular shock reformation in two-dimensional hybrid simulations. 36, L05103. doi:10.1029/2008GL036675.